Draft version October 22, 2026
Typeset using LaTeX **twocolumn** style in AASTeX7.0.1

arXiv:2610.29137v1 [astro-ph.GA] 21 Oct 2026

NGC 3227 Blinks: An Extreme Changing-Look Event in a Seyfert Galaxy

Kaiwen Zhang,[1] Michael S. Brotherton,[1] Pu Du,[2] Dong-Wei Bao,[2,3] Bi-Xuan Zhao,[2] Feng-na Fang,[2] Yan-Rong Li,[2] Chen Hu,[2] Ming Xiao,[2] Keith Horne,[4] Gerard A. Kriss,[5] Daniel Proga,[6] and Jian-Min Wang[2,3,7]

[1] *Department of Physics and Astronomy, University of Wyoming, Laramie, WY 82071, USA*
[2] *Key Laboratory for Particle Astrophysics, Institute of High Energy Physics, Chinese Academy of Sciences, 19B Yuquan Road, Beijing 100049, P. R. China*
[3] *School of Astronomy and Space Science, School of Physical Sciences, University of Chinese Academy of Sciences, 19A Yuquan Road, Beijing 100049, P. R. China*
[4] *SUPA School of Physics and Astronomy, North Haugh, St. Andrews, KY16 9SS, Scotland, UK*
[5] *Space Telescope Science Institute, 3700 San Martin Dr., Baltimore, MD 21218, USA*
[6] *Department of Physics & Astronomy, University of Nevada, Las Vegas, 4505 S. Maryland Pkwy, Las Vegas, NV 89154-4002, USA*
[7] *National Astronomical Observatories of China, Chinese Academy of Sciences, 20A Datun Road, Beijing 100020, P. R. China*

Submitted to ApJL

ABSTRACT

We report a rapid optical changing-look event in the Seyfert galaxy NGC 3227: the optical continuum faded by ∼70% and broad Hβ emission nearly disappeared within weeks, before recovering within two months. Damped random walk simulations calibrated to the source's normal variability show that such a decline is unlikely for stochastic accretion fluctuations. The optical decline coincides with an X-ray spectral hardening event detected by *Swift*, indicating additional line-of-sight absorption. During the dim state, reverberation mapping yields a clear 6–8 day lag between the continuum and broad Hβ, placing the obscurer interior to the broad-line region. Photoionization calculations require a fully ionized Compton-thick column with $N_{\rm H} \approx 1.5 \times 10^{24}\,{\rm cm}^{-2}$ to reproduce the optical continuum suppression. Together, these observations demonstrate that compact, high-column-density obscurers interior to the broad-line region can produce extreme optical changing-look behavior on timescales of weeks.

Keywords: Active galactic nuclei (16) — Seyfert galaxies (1447) — Reverberation mapping (2019) — Supermassive black holes (1663) — Quasars (1319)

1. INTRODUCTION

Changing-look active galactic nuclei (CLAGNs) are AGNs that exhibit dramatic changes in their spectral characteristics (C. Ricci & B. Trakhtenbrot 2023), such as the appearance or disappearance of broad emission lines or changing X-ray spectral slopes. Changing-look events provide direct probes of changes in the inner accretion flow, the formation and destruction of circumnuclear structures, and the gaseous environment surrounding AGNs.

These transitions are generally attributed to two distinct physical mechanisms (C. Ricci & B. Trakhtenbrot 2023). In the first case, changes in the intrinsic accretion flow onto the supermassive black hole (SMBH) lead to the strengthening or weakening of the ionizing continuum, resulting in the appearance or disappearance of broad emission lines (J. C. Runnoe et al. 2016; M. J. Graham et al. 2020). In the second, known as changing obscuration, variations in the line-of-sight column density modulate the observed emission, producing pronounced spectral changes (G. Risaliti et al. 2009; G. Torricelli-Ciamponi et al. 2014). Such obscuration-driven events display X-ray spectral hardening, often accompanied by suppressed soft X-ray emission and, in some cases, blue-shifted broad absorption-line troughs in the ultraviolet (A. King & K. Pounds 2015; J. S. Kaastra et al. 2014).

While most optical CLAGN events are attributed to intrinsic accretion-rate changes (C. Ricci & B. Trakhtenbrot 2023; A. Jana et al. 2025; M. J. Temple et al.

Email: kzhang1@uwyo.edu

2022), direct evidence that obscuration alone can drive large-amplitude optical continuum and broad emission-line variability has been reported in only a few cases (G. Zeltyn et al. 2022; V. L. Oknyansky et al. 2021; X. Zhang 2026).

NGC 3227 is a nearby, well-studied Seyfert galaxy ($z = 0.003859$) at a distance of 23.7 Mpc (M. C. Bentz et al. 2023), with a black hole mass of $M_{\rm BH} \sim 1\times10^7\ M_\odot$ from reverberation mapping (M. S. Brotherton et al. 2020; M. C. Bentz et al. 2023) and dynamical modeling (M. C. Bentz et al. 2023; V. N. Bennert et al. 2026). It is in an early-stage interaction with its companion, NGC 3226. This interaction has resulted in substantial internal reddening in the host galaxy of NGC 3227, as revealed by H I radio mapping (C. G. Mundell et al. 1995) and by the reddened optical and ultraviolet spectral shape (D. M. Crenshaw et al. 2001; M. Mehdipour et al. 2021). We account for this reddening in our spectral decomposition (Section 3.1).

NGC 3227 has a long history of X-ray variability and obscuration events, with episodes of X-ray spectral hardening reported as early as 2000 using *RXTE* observations (G. Lamer et al. 2003; A. G. Markowitz et al. 2014). Subsequent X-ray monitoring has revealed additional hardening events (A. G. Markowitz et al. 2014; T. Beuchert et al. 2015; T. J. Turner et al. 2018; Y. Wang et al. 2022), suggesting that such obscuration events recur. However, none of these episodes was accompanied by high-cadence optical spectroscopic monitoring.

In November 2019, another X-ray hardening event in NGC 3227 was detected by *Swift* (M. Mehdipour et al. 2021), triggering intensive multi-wavelength follow-up observations with *HST*, *XMM-Newton*, and *NuSTAR*. During this campaign, the nucleus exhibited a pronounced decline in flux from the UV to the X-ray bands, with the suppression strongest at soft X-ray energies, consistent with the appearance of new obscuring gas along the line of sight (M. Mehdipour et al. 2021). Between the two target-of-opportunity epochs, the obscurer column density increased from $N_{\rm H} \sim 10^{22}$ cm^{-2} in mid-November to $\sim 10^{23}$ cm^{-2} by early December, tracking the deepening X-ray suppression (J. Mao et al. 2022).

In this Letter, we present contemporaneous high-cadence optical spectroscopic monitoring of NGC 3227 that covers this event. We describe the observations and data reduction in Section 2, the spectral analysis in Section 3, and our results in Section 4, comprising the changing-look event itself, a damped random walk null test, the reverberation analysis, and photoionization modeling of the obscurer. We discuss the implied obscuration geometry in Section 5 and summarize in Section 6.

2. OBSERVATIONS AND DATA REDUCTION

2.1. *WIRO spectroscopic monitoring*

We monitored NGC 3227 between 2019 November 14 and 2020 May 29 with the Wyoming Infrared Observatory (WIRO) 2.3 m telescope using the Long Slit Spectrograph in remote-operation mode (J. R. Findlay et al. 2016), following the procedures established for the Monitoring AGNs with Hβ Asymmetry (MAHA) campaigns (P. Du et al. 2018). The 900 line mm^{-1} grating provided a dispersion of 1.49 Å pixel^{-1} over 4000–7000 Å. Observations were carried out with a 5″ wide slit fixed in the north–south orientation. Each epoch typically consisted of three 5 minute exposures. At least one spectrophotometric standard star (usually Feige 34, occasionally G191B2B) was observed per night, along with CuAr lamps for wavelength calibration and dome flats from a uniformly illuminated white card.

Data were reduced following the standard MAHA pipeline (P. Du et al. 2018), which employs IRAF v2.16 (D. Tody 1986, 1993) for the basic reduction steps. One-dimensional spectra were extracted with apertures of ±6.″8 and background windows spanning 7.″6–15.″1 on both sides. Flux calibration and extinction correction were applied using spectrophotometric standards, but additional corrections were required to account for variable atmospheric transparency and telescope tracking errors.

We adopted the [O III] λ5007 narrow-line emission as an internal flux calibrator, since it originates from an extended narrow-line region that is stable on timescales of years (B. M. Peterson et al. 2013). Variable seeing and tracking errors between epochs introduce small shifts in the [O III] line centroid, which would propagate into the flux calibration. To mitigate this, all spectra were convolved to a common spectral resolution before calibration. This reduces the effective spectral resolution but does not affect the broad-line measurements that are the focus of this work. Relative spectrophotometric calibration was then performed using the algorithm of E. van Groningen & I. Wanders (1992), with minor modifications (P. Du et al. 2018). We measured the [O III] fluxes over 5005–5050 Å from spectra obtained under photometric conditions. Final flux-calibrated spectra were obtained by noise-weighted averaging of exposures from the same night.

2.2. *Archival ZTF photometry*

To supplement the continuum light curve and increase the sampling cadence, we used archival g-band photometry of NGC 3227 from the Zwicky Transient Facility (ZTF; IRSA 2022). The data were extracted from a region centered on the nucleus,

with only measurements having `catflag` = 0 retained for quality control. All data were drawn from object IDs 571109400017782, 572112300010962, and 1617102200002807, covering the heliocentric Julian date (HJD) range 2458800 to 2459010.

The inter-calibration between the ZTF g-band light curve and the WIRO spectroscopic photometry at 5100 Å was performed using `PyCALI` (Y.-R. Li et al. 2014). Before calibration, the ZTF observations were rebinned by averaging all measurements within a single day, and three binned epochs exceeding 3σ from the reconstructed light curve were removed to improve data quality.

3. SPECTRAL ANALYSIS

3.1. *Host decomposition and reddening correction*

The reduced spectra of NGC 3227 were corrected for Milky Way extinction using the G23 extinction curve of K. D. Gordon et al. (2023) with $R_V = 3.1$ and $E(B-V) = 0.02$ mag, then shifted to the rest frame. The AGN and host galaxy contributions were separated using spectral decomposition with the galaxy templates of A. L. Kinney et al. (1996). The final host spectrum was constructed as a linear combination of Sa, Sb, and bulge templates with scaling factors of 1/10.9, 1/8.3, and 1/100, respectively. These factors were fixed by two joint requirements: (i) the residual AGN continuum remains non-negative in the lowest-flux state, and (ii) the host stellar absorption features — in particular the Na I D doublet near 5900 Å — are removed in the residual AGN spectra. The host contribution is dominated by the Sa and Sb components, with a negligible bulge contribution. This host spectrum, assumed constant across epochs, was subtracted from all spectra.

NGC 3227 is known to suffer significant internal reddening (D. M. Crenshaw et al. 2001; C. G. Mundell et al. 1995). Following M. Mehdipour et al. (2021), we applied the SMC Bar extinction curve of K. D. Gordon et al. (2003) with $R_V = 4.0$ and $E(B-V) = 0.45$ mag, which they found to best characterize the dust extinction in the nuclear region. The AGN-only spectra were dereddened using this extinction curve to recover the intrinsic AGN continuum and emission-line fluxes.

3.2. *Mean and rms spectra*

We constructed mean and root-mean-square (rms) spectra from the reddening-corrected AGN spectra to characterize the average emission profile and its variability. Integration windows were then defined for the Hβ emission line and the [O III] $\lambda\lambda$4959, 5007 doublet, with boundaries set from the extent of the line emission in the mean and rms spectra. The Hβ profile was measured over 4800–4929 Å, the [O III] doublet over 4929–5040 Å, and the 5100 Å continuum over 5075–5125 Å. The minimal [O III] in the rms spectrum confirms the stability of the flux calibration. The mean and rms spectra, together with the wavelength windows defined above, are shown in Figure 1.

3.3. *Recovery of the broad Hβ component*

To remove the local AGN continuum around the Hβ line, we defined continuum windows on either side of the Hβ+[O III] complex, specifically 4750–4790 Å and 5075–5125 Å. These windows were chosen to coincide with line-free regions in the mean and rms spectra, as identified by visual inspection. The local continuum was then modeled by linear interpolation between the two windows, and subtracted to isolate the emission-line flux. The continuum-subtracted spectra showing the broad Hβ variability and the stable [O III] doublet across all monitoring epochs are shown in Figure 2.

The broad Hβ component was deblended by subtracting the narrow-line contribution from the continuum-subtracted Hβ emission region. The narrow Hβ flux and profile were assumed to be stable during the monitoring campaign, as indicated by the constancy of the [O III] emission line. To determine the narrow Hβ profile, we used a low-state spectrum (2019 December 19) to minimize contamination from the broad Hβ component and residual continuum. Emission-line profiles were modeled using a Markov chain Monte Carlo (MCMC) approach to fully explore the parameter space of the broad and narrow components. The fitting was restricted to a narrow wavelength interval of 4840–4880 Å. This restriction is required because the broad Hβ emission exhibits complex substructure in the lowest state that cannot be adequately represented by a single Gaussian; fitting the full profile would otherwise bias the decomposition by allowing the broad component to dominate the χ^2 minimization. The posterior distributions for the narrow Hβ component yield amplitude $A = 2.75^{+0.21}_{-0.24} \times 10^{-14}$ erg cm^{-2} s^{-1} Å^{-1}, mean $\mu = 4860.62^{+0.24}_{-0.23}$ Å, and width $\sigma = 8.74^{+0.69}_{-0.62}$ Å. The broad Hβ profiles were then recovered by subtracting the best-fitting narrow component from the observed spectra. The resulting narrow-line flux ratio of [O III] λ5007/H$\beta \approx 9$ is consistent with the typical value of $\sim$10 observed among AGNs (L. J. Kewley et al. 2006; J. Stern & A. Laor 2013), supporting the robustness of the decomposition.

3.4. *Light curves*

Given the complex structure of the Hβ profile, the broad Hβ flux in the WIRO spectra was measured by direct integration over the recovered broad-line spectrum

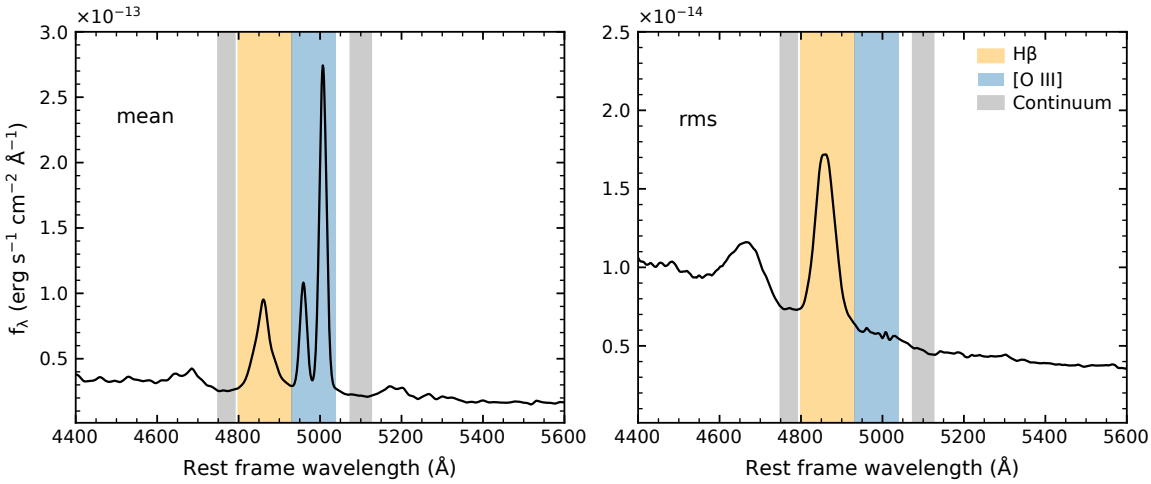


Figure 1. Mean and rms spectra from the WIRO monitoring campaign of NGC 3227. Left: mean spectrum. Right: rms spectrum. The gray region marks the local continuum window used for Hβ pseudo-continuum subtraction, the orange region marks the Hβ measurement window (4800–4929 Å), and the cyan region marks the [O III] $\lambda\lambda$4959, 5007 doublet (4929–5040 Å). The minimal [O III] variability in the rms spectrum confirms the stability of the flux calibration.

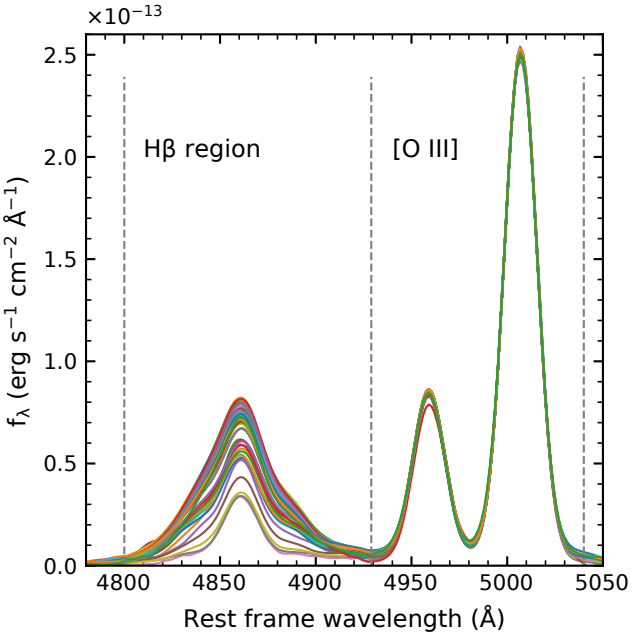


Figure 2. Continuum-subtracted Hβ and [O III] emission–line profiles, one colored curve per epoch of the 2019–2020 campaign, after subtraction of the host galaxy and a local linear continuum (windows at 4750–4790 and 5075–5125 Å). The Hβ profile, containing both broad and narrow-line components, varies by more than a factor of two between epochs, while the narrow [O III] $\lambda\lambda$4959, 5007 doublet stays essentially constant, confirming [O III] as a stable internal flux reference. Vertical dashed lines mark the Hβ (4800–4929 Å) and [O III] (4929–5040 Å) windows.

within the Hβ window. The 5100 Å continuum flux was estimated as the mean flux density within the 5075–5125 Å continuum window. The total uncertainties consist of two components: Poisson noise from the observations and systematic uncertainties. Poisson noise was propagated throughout the data analysis. Systematic uncertainties were estimated using two complementary approaches, combined in quadrature, following standard MAHA practices (P. Du et al. 2018; M. S. Brotherton et al. 2020). The first quantifies within-night variations: for epochs with multiple exposures, the scatter among individual flux measurements captures the effect of changing atmospheric conditions and tracking errors. The second captures short-term variability across epochs: the light curve is smoothed with a five-point median filter (P. Du et al. 2014, 2015), and the standard deviation of the residuals provides an estimate of rapid intrinsic fluctuations. The resulting broad Hβ and 5100 Å continuum light curves are shown in Figure 3.

4. RESULTS

4.1. *An extreme optical changing-look event*

Our optical spectroscopic monitoring with WIRO, which overlaps with the 2019 November multi-wavelength campaign, shows a contemporaneous decline in optical flux that evolves on weekly timescales (Figure 3). The AGN optical continuum at 5100 Å and the broad Hβ light curve show substantial declines of approximately 70% and 80%, respectively. The broad Hβ profile nearly disappears in the low state (2019 December 19) and recovers by the high state (2020 January 31), while the narrow Hβ emission remains unchanged throughout. **T**he *Swift*/XRT hardening began before the first WIRO epoch and continued through the early optical drop. During the period of joint coverage, both the optical continuum and the *Swift*/XRT count rates

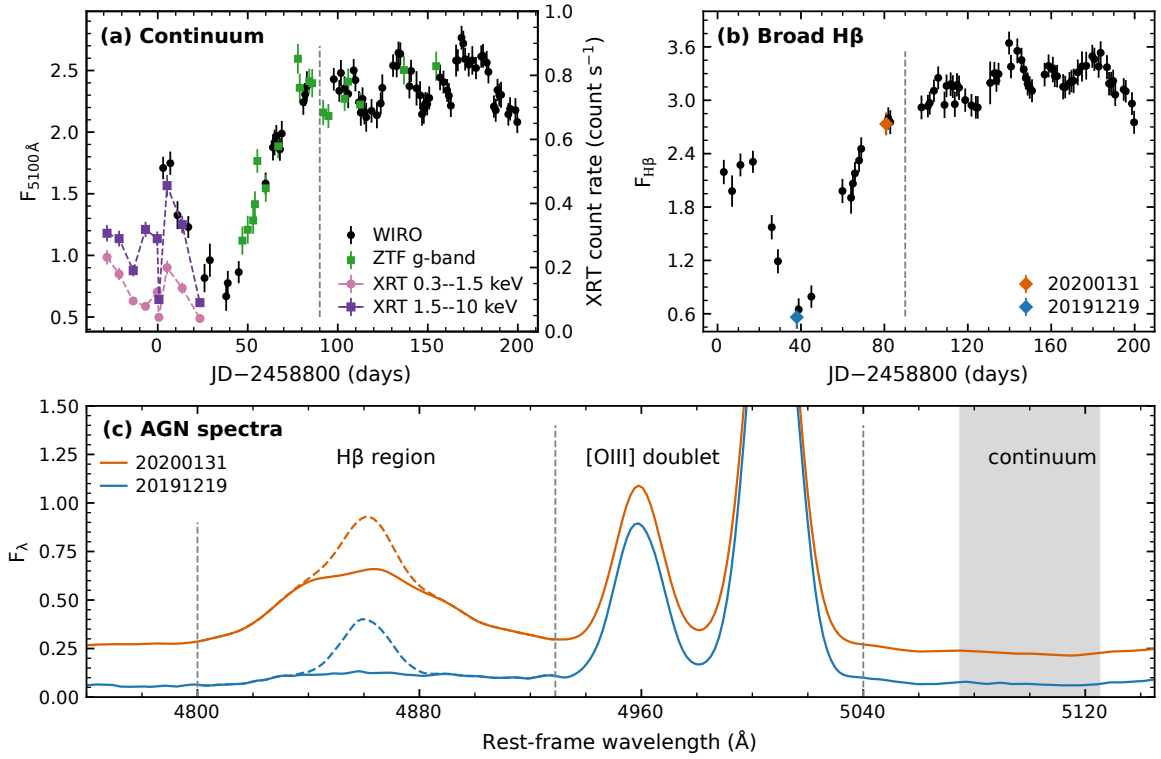


Figure 3. Optical continuum, Swift/XRT, and broad Hβ variability in NGC 3227. (a) Light curve of the rest-frame 5100 Å AGN continuum in units of 10^{-14} erg cm^{-2} s^{-1} Å^{-1}. Black points show WIRO measurements, while green points indicate ZTF g-band photometry inter-calibrated to the WIRO 5100 Å flux scale. Pink and purple points show the *Swift*/XRT 0.3–1.5 and 1.5–10 keV count rates, respectively, from J. Mao et al. (2022) (right-hand axis, in count s^{-1}); dashed lines connect consecutive epochs. The vertical dashed line at 90 days marks the transition from the obscuration phase to the subsequent normal phase. (b) Broad Hβ emission-line light curve from WIRO spectroscopy in units of 10^{-12} erg cm^{-2} s^{-1}. Colored points highlight epochs corresponding to the spectra shown in panel (c), using the same color coding. (c) Representative AGN intrinsic spectra in the low state (2019 December 19; blue) and high state (2020 January 31; orange) in units of 10^{-14} erg cm^{-2} s^{-1} Å^{-1}. The Hβ region and the [O III] doublet are shown. Dashed curves indicate the narrow-line Hβ emission, while solid curves represent the spectrum after Hβ narrow-line subtraction. Vertical dashed lines mark the boundaries of the Hβ and [O III] doublet regions. The gray shaded region marks the 5100 Å continuum flux at the given epochs.

declined, though the X-ray sampling is sparse and ends prior to the optical minimum. The overlapping X-ray hardening supports a physical association with the optical decline, but we cannot conclusively demonstrate that both behaviors were produced by the exact same obscuring structure.

Given this rapid decline in continuum flux, stochastic accretion variability alone is an unlikely explanation: only ∼0.2% of damped random walk simulations calibrated to NGC 3227's normal-state variability reproduce a decline this steep (Section 4.3). Combined with the X-ray hardening at the onset of the optical decline, we argue that this event is driven by obscuration. Reverberation mapping through the dim state (Section 4.2) recovers a robust 6–8 day lag between the continuum and broad Hβ, showing that the broad-line region continues to reverberate and placing the obscuring material interior to the broad-line region.

4.2. *Reverberation lags*

We divided the light curves into two temporal segments. The obscuration phase (2019 November 14 to 2020 January 31) captures the sharp decline in Hβ flux, following an X-ray hardening event, and its subsequent recovery. The normal phase (2020 February 2 to 2020 May 29) reflects typical AGN stochastic variability.

We employed the interpolated cross-correlation function (ICCF; C. M. Gaskell & L. S. Sparke 1986), implemented with the `PyCCF` package (M. Sun et al. 2018), to estimate the time lag between the ionizing continuum and the Hβ emission line, thereby inferring the broad-line region (BLR) size via the light-travel distance. To complement this classical approach, we also applied Multiple and Inhomogeneous Component Analysis (MICA; Y.-R. Li et al. 2016), a Bayesian reverberation-mapping framework. MICA simultaneously models the

stochastic continuum and the line response using a flexible transfer-function parameterization.

To improve coverage during the obscuration phase, we augmented the 5100 Å continuum with inter-calibrated ZTF data, as sparse sampling degrades both ICCF and MICA results more than the modest systematics introduced by inter-calibration. In contrast, ZTF data were excluded from the normal phase to preserve the homogeneity and precision of our primary dataset, though including the inter-calibrated ZTF data in the normal phase yields an essentially identical lag. ICCF and MICA analyses were performed independently for each phase, enabling a direct comparison of the delay behavior.

During the obscuration phase (Figure 4), the ICCF centroid distribution gives a lag of $6.13^{+1.44}_{-0.99}$ days, while MICA yields a broader posterior at $7.72^{+2.09}_{-2.10}$ days. During the normal phase (Figure 5), ICCF analysis yields a lag of $4.99^{+1.53}_{-1.43}$ days and MICA gives $5.38^{+0.87}_{-0.88}$ days; both methods converge on a consistent lag of ∼5 days, indicating a relatively stable BLR response under unobscured conditions and consistent with previous reverberation mapping results for NGC 3227 (M. C. Bentz et al. 2023; M. S. Brotherton et al. 2020).

4.2.1. *Robustness of the obscuration-phase lag*

To assess whether the deep-valley shape and reduced cadence of the obscuration phase could bias the recovered lag, we performed mock recovery tests using ICCF. We treated the MICA-reconstructed mean continuum light curve as the deterministic "true" continuum, convolved it with a Gaussian transfer function of standard deviation $\sigma \approx 1.67$ days to generate an Hβ light curve, interpolated both at the actual observation epochs, and assigned per-epoch uncertainties by rescaling the observed flux errors so that each mock point preserves the fractional uncertainty of the corresponding real measurement. We tested two input lags: $\tau_0 = 0$ (null) and $\tau_0 = 6$ days (recovery). ICCF recovered both inputs within their quoted uncertainties ($\tau = 0.11^{+0.94}_{-0.53}$ d for $\tau_0 = 0$ and $\tau = 5.50^{+0.98}_{-0.97}$ d for $\tau_0 = 6$ d), demonstrating that the obscuration-phase lag is not a spurious artifact of the sampling. Drawing pairs from the observed and mock zero-lag cross-correlation centroid distributions, we find $p(\tau_{\rm null} \geq \tau_{\rm obs}) \approx 6.8 \times 10^{-5}$, equivalent to a 3.8σ rejection of the null hypothesis $\tau = 0$; the observed lag distribution is therefore inconsistent with arising from a zero-lag light curve under the actual sampling and noise.

4.3. *Damped random walk null test*

To assess whether the observed ∼70% optical continuum decline could arise from stochastic accretion fluctuations rather than an external obscuration event, we performed a null-hypothesis test using damped random walk (DRW) simulations.

We used five seasons of MAHA optical monitoring of NGC 3227 obtained outside the obscuration episode: the 2017 season (M. S. Brotherton et al. 2020) and four subsequent seasons spanning 2019–2023 (Zhang et al. 2027, MAHA VI, in preparation). A monotonically declining segment of the 2023 season was excluded to ensure that the DRW parameters reflect stochastic variability. For each season, we independently inferred the DRW parameters, σ (variability amplitude) and τ (characteristic timescale), and combined the posterior samples to determine representative median values. We obtained $\tau = 9.66^{+8.89}_{-3.69}$ days and $\sigma = 3.63^{+1.87}_{-1.67} \times 10^{-15}$ erg cm^{-2} s^{-1} Å^{-1}.

Using these median parameters, we generated 100,000 mock light curves drawn from a DRW Gaussian process, adopting the same temporal sampling and photometric uncertainties as during the monitoring campaign. For each realization, we searched for events that exhibited a ≥70% decline in continuum flux on timescales shorter than 40 days. Such events occur in only 0.2% of the simulated light curves, and only a similarly small fraction of light curves would recover to a high state on the same timescale. This low occurrence rate indicates that the observed continuum drop and subsequent rise is very unlikely to arise from stationary stochastic accretion variability alone.

4.4. *Photoionization modeling of the obscurer*

The host-galaxy subtracted rest-frame 5100 Å continuum flux drops from 2.24×10^{-14} to 6.68×10^{-15} erg cm^{-2} s^{-1} Å^{-1} between the high and low states, a decline of ∼70%. To interpret this attenuation, we performed photoionization modeling with `Cloudy` C25 (C. M. Gunasekera et al. 2025) to identify the obscurer column density required to reproduce the observed low-state 5100 Å flux. The ionizing source was modeled with the intrinsic AGN spectral energy distribution of NGC 5548 (Mehdipour, M. et al. 2015), normalized to the high-state luminosity $\lambda L_{5100\,\text{Å}} \simeq 7.76 \times 10^{42}$ erg s^{-1}. The obscurer was modeled as a plane-parallel slab of solar-abundance gas.

The exact location and density of the obscurer are not directly constrained by our data; therefore, we choose sampling ranges that are physically plausible for an obscurer interior to the 5100 Å continuum-emitting region. Following the disk size–luminosity relation of C. J. Burke et al. (2021), the characteristic 2500 Å emitting radius of NGC 3227 is ∼0.09 light-days, and the empirical continuum reverberation scaling $\tau \propto \lambda^{4/3}$ (R. Edelson et al. 2015; M. M. Fausnaugh et al. 2016) extrap-

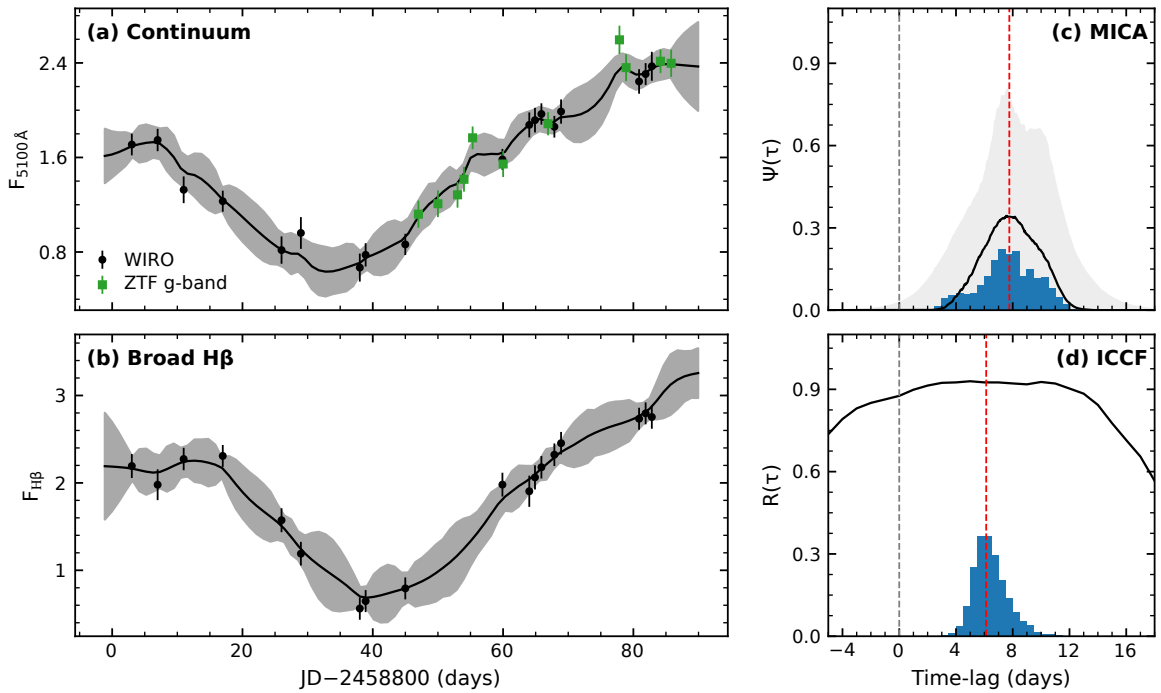


Figure 4. Time-lag analysis of the continuum and broad Hβ emission during the obscuration phase. Panels (a) and (b) show the observed (points) and MICA-reconstructed light curves of the rest-frame 5100 Å continuum and the broad Hβ emission, in units of 10^{-14} erg cm^{-2} s^{-1} Å^{-1} and 10^{-12} erg cm^{-2} s^{-1}, respectively. Solid black curves trace the median reconstructed light curve and gray bands show its 1σ uncertainty. The 5100 Å continuum in panel (a) is supplemented with the inter-calibrated ZTF g-band photometry (green points). Panel (c) shows the MICA lag posterior distribution (histogram); the solid black curve is the median reconstructed transfer function and the gray band marks its 1σ uncertainty. Panel (d) shows the ICCF centroid distribution (histogram) together with the cross-correlation function (solid black curve). Vertical red dashed lines mark the median lag values. The MICA lag posterior distribution has a median of ∼7.7 d, while the ICCF centroid distribution has a median value of ∼6 d.

olates this to ∼0.23 light-days at 5100 Å. We therefore sampled obscurer inner radii of $r = 0.1$–0.2 light-days, just interior to the 5100 Å emitting region, and hydrogen number densities $\log(n_{\rm H}/{\rm cm}^{-3}) = 9$–$10$, typical of gas at BLR scales (B. M. Peterson 2006).

We performed grid photoionization modeling over this parameter space, with column densities spanning $\log(N_{\rm H}/{\rm cm}^{-2}) = 23$–$24.5$. Across this grid the ionization parameter spans $\log U \approx 3$–4.5, leaving the obscurer fully ionized in all cases. The transmitted 5100 Å flux therefore depends only on $N_{\rm H}$, with negligible sensitivity to $n_{\rm H}$ or r. The `Cloudy` results coincide with the analytic Thomson prediction $T = \exp(-1.17\, N_{\rm H}\, \sigma_{\rm T})$ for fully ionized hydrogen + helium gas at solar abundance, confirming that bound-free and line opacities are negligible at optical wavelengths and that electron scattering accounts for the entire attenuation. Reproducing the observed flux decrease requires a Compton-thick column density of $N_{\rm H} \simeq 1.5 \times 10^{24}$ cm^{-2}. Across the explored `Cloudy` grid, energy is conserved to within ∼3%; at the best-fit column the obscurer's diffuse outward continuum at 5100 Å remains below $\sim 4 \times 10^{-4}$ of the transmitted flux, confirming that the fully ionized cloud does not self-illuminate the optical band probed in this work.

5. DISCUSSION

The detection of a coherent reverberation lag between the continuum and broad Hβ during the obscuration phase localizes the obscuring material: the Hβ decline is the BLR's light-travel response to an attenuated ionizing continuum, not a direct extinction of the line-emitting gas along our sightline, so the BLR continues to reprocess the continuum it receives. This excludes obscuration exterior to the BLR. Such an obscurer dims Hβ only by attenuating the line emission, so suppressing the broad Hβ flux by ∼80% requires it to cover most of the spatially extended BLR — a structure comparable in scale to the BLR itself. If the obscurer covers the continuum source and BLR simultaneously (for example, an in-situ rise in opacity along the sightline), the two decline together, producing correlated, zero-lag drops.

If instead the obscurer transits the system, it occults the continuum source and the surrounding BLR at different times and smears the Hβ decline over the crossing — in neither case reproducing the coherent ∼6–8 day

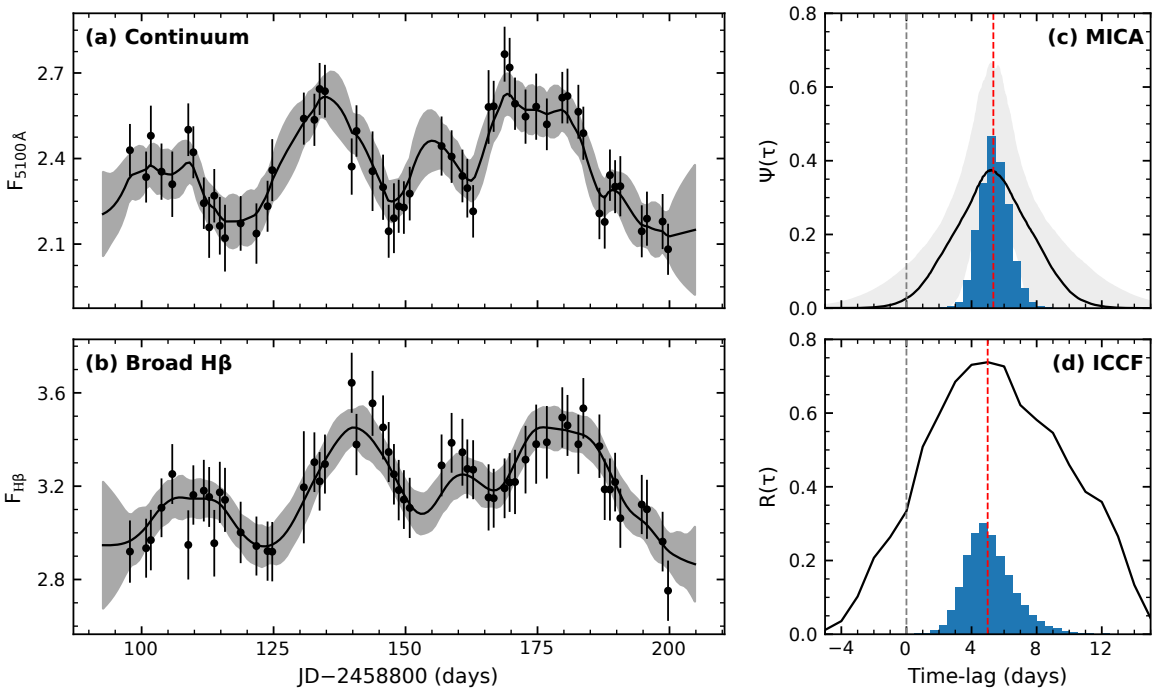


Figure 5. Time-lag analysis of the continuum and broad Hβ emission during the normal phase. Same as Figure 4, but for the normal phase. Both methods yield a consistent reverberation lag of ∼5 d, with the MICA lag posterior distribution having a median of ∼5.4 d, indicating a stable broad-line region response under presumably unobscured conditions.

delay we observe. A well-defined positive lag, in which the entire Hβ light curve follows the continuum after a fixed delay, is instead the signature of light-travel reprocessing and requires the obscurer to lie interior to the BLR, where it attenuates the continuum before it reaches the line-emitting gas. This inner location is consistent with the X-ray analysis of the 2019 event by J. Mao et al. (2022), and with this system's earlier X-ray occultations, whose absorbing clouds were also placed within or at the inner edge of the BLR (T. J. Turner et al. 2018; T. Beuchert et al. 2015).

Photoionization modeling further shows that reproducing the observed attenuation of the 5100 Å continuum requires a fully ionized Compton-thick column density of $N_{\rm H} \sim 1.5 \times 10^{24}$ cm^{-2} along the line of sight. Such a large column density is qualitatively consistent with the pronounced soft X-ray suppression and X-ray spectral hardening observed at the onset of this event, although the X-ray-derived column density is one to two orders of magnitude lower. This difference likely reflects both temporal and geometric factors: the X-ray column was likely still *evolving* when last measured, increasing from $\sim 10^{22}$ to $\sim 10^{23}$ cm^{-2} over the weeks before the optical minimum (J. Mao et al. 2022), and no X-ray observation samples the epoch of deepest optical suppression (2019 December 19, both later and deeper than the final X-ray epoch), precluding a direct comparison at the same evolutionary stage. Furthermore, the X-ray column density traces a narrow sightline to the compact corona, whereas the optical continuum sees a sightline to the continuum source at a larger radius, where the obscurer's column density may differ.

To illustrate the observational results, we present a proposed obscuration geometry in Figure 6, which is similar to that previously offered for Mrk 817 (E. Kara et al. 2021), where a comparable inner obscurer left the broad UV lines decoupled from the observed continuum (a "holiday"; Y. Homayouni et al. 2024). In NGC 3227 the covering instead suppresses the continuum reaching the Hβ-emitting BLR, producing a full Hβ changing-look event. Unlike the Mrk 817 holiday, however, the persistent ∼6–8 day lag shows that Hβ still reverberates in response to the attenuated continuum. The physical nature of the obscurer — whether a disk wind or another circumnuclear structure — cannot be determined from the present data and remains an open question. We note, however, that a time-dependent, line-driven accretion-disk wind is one plausible candidate: simulations show that such winds can become Compton-thick along equatorial sightlines (D. Proga et al. 2000; D. Proga & T. R. Kallman 2004).

The event in NGC 3227 is currently unique in exhibiting X-ray obscuration accompanied by an optical changing-look transition, in which the broad emission lines nearly vanished alongside the continuum. In contrast, most X-ray changing-obscuration events

do not show a clear correlation between the X-ray and UV/optical changing-look behavior. Certain X-ray changing-obscuration events (e.g., Mrk 817 and NGC 5548) instead exhibit (a) blueshifted absorption-line troughs rather than the near-complete continuum and emission-line suppression observed here, and (b) a BLR "holiday," in which the broad lines decouple from the ionizing-continuum variability (M. R. Goad et al. 2016; M. Dehghanian et al. 2019; E. Kara et al. 2021; Y. Homayouni et al. 2024). Such holidays may depend on the obscurer's column density ($N_{\rm H}$): if the material is transparent to specific bands of the spectral energy distribution, only partial suppression occurs. Because Compton-thick, near-total-coverage obscuration events are likely far rarer than ordinary obscuration, NGC 3227 remains the only unambiguous case identified to date.

6. SUMMARY

We have presented high-cadence optical spectroscopic monitoring of an extreme changing-look event in NGC 3227 and shown that: (1) the 5100 Å continuum and broad Hβ flux fell by ∼70% and ∼80% and recovered within two months, a decline that damped random walk simulations disfavor as stochastic accretion variability ($p = 0.002$) and that coincides with *Swift* X-ray hardening; (2) a persistent 6–8 day continuum-to-Hβ lag through the dim state shows the broad-line region still reverberates, placing the obscurer interior to the BLR; and (3) reproducing the optical suppression requires a fully ionized, Compton-thick column, $N_{\rm H} \simeq 1.5 \times 10^{24}\,{\rm cm}^{-2}$. Together these establish that compact, high-column-density obscuration interior to the BLR can drive an extreme optical changing-look event on week timescales. Such events are hard to characterize from either band alone — X-ray and UV data fix the absorber's column and ionization state, high-cadence optical spectroscopy localizes it through reverberation mapping — so simultaneous coverage is needed to constrain the obscurer's geometry. Wide-field time-domain surveys with the Rubin Observatory should uncover many more and motivate the coordinated follow-up such events require.

ACKNOWLEDGMENTS

We thank the WIRO engineering staff James Weger and Conrad Vogel for their dedicated technical support in maintaining the telescope and instrumentation that made these observations possible. Based on observations obtained with the Samuel Oschin Telescope 48 inch and the 60 inch Telescope at the Palomar Observatory as part of the Zwicky Transient Facility project. ZTF is supported by the National Science Foundation under Grants No. AST-1440341 and AST-2034437 and a collaboration including current partners Caltech, IPAC, the Weizmann Institute for Science, the Oskar Klein Center at Stockholm University, the University of Maryland, Deutsches Elektronen-Synchrotron and Humboldt University, the TANGO Consortium of Taiwan, the University of Wisconsin at Milwaukee, Trinity College Dublin, Lawrence Livermore National Laboratories, IN2P3, University of Warwick, Ruhr University Bochum, Northwestern University and former partners the University of Washington, Los Alamos National Laboratories, and Lawrence Berkeley National Laboratories. Operations are conducted by COO, IPAC, and UW.

This work was supported by the U.S. National Science Foundation through grant AST-2511198. P.D. acknowledges financial support from the National Key R&D Program of China (2023YFA1607903 and 2021YFA1600404), from NSFC grants NSFC-12521005, -12022301 and -11991051, the National Science and Technology Major Project (2024ZD0300303), and by the China Manned Space Project with no. CMS-CSST-2025-A07.

Facilities: WIRO (Wyoming Infrared Observatory), ZTF (Zwicky Transient Facility), Swift

Software: Cloudy (C. M. Gunasekera et al. 2025), IRAF (D. Tody 1986, 1993), MICA (Y.-R. Li et al. 2016), PyCALI (Y.-R. Li et al. 2014), PyCCF (M. Sun et al. 2018)

DATA AVAILABILITY

The underlying data, light curves, spectra, and processing/analysis scripts used to produce the figures and results presented in this manuscript are available via DOI: 10.5281/zenodo.23191065.

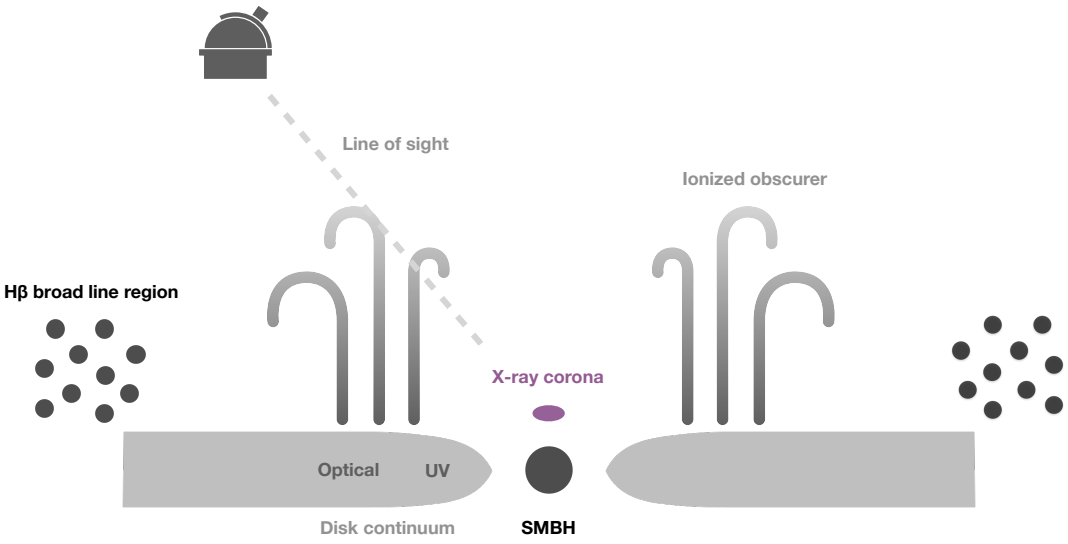


Figure 6. Schematic illustration of the proposed obscuration geometry in NGC 3227. A dense, Compton-thick obscuring structure located interior to the BLR rises above the accretion disk, blocking the ionizing continuum before it reaches the BLR while also attenuating the observed 5100 Å optical continuum along our line of sight.

REFERENCES

Bennert, V. N., Winkel, N., Treu, T., et al. 2026, ApJ, 1000, 48, doi: 10.3847/1538-4357/ae41ad

Bentz, M. C., Markham, M., Rosborough, S., et al. 2023, ApJ, 959, 25, doi: 10.3847/1538-4357/ad08b8

Beuchert, T., Markowitz, A. G., Krauß, F., et al. 2015, A&A, 584, A82, doi: 10.1051/0004-6361/201526790

Brotherton, M. S., Du, P., Xiao, M., et al. 2020, ApJ, 905, 77, doi: 10.3847/1538-4357/abc2d2

Burke, C. J., Shen, Y., Blaes, O., et al. 2021, Science, 373, 789, doi: 10.1126/science.abg9933

Crenshaw, D. M., Kraemer, S. B., Bruhweiler, F. C., & Ruiz, J. R. 2001, ApJ, 555, 633, doi: 10.1086/321522

Dehghanian, M., Ferland, G. J., Peterson, B. M., et al. 2019, ApJL, 882, L30, doi: 10.3847/2041-8213/ab3d41

Du, P., Hu, C., Lu, K.-X., et al. 2014, ApJ, 782, 45, doi: 10.1088/0004-637X/782/1/45

Du, P., Hu, C., Lu, K.-X., et al. 2015, ApJ, 806, 22, doi: 10.1088/0004-637X/806/1/22

Du, P., Brotherton, M. S., Wang, K., et al. 2018, ApJ, 869, 142, doi: 10.3847/1538-4357/aaed2c

Edelson, R., Gelbord, J. M., Horne, K., et al. 2015, ApJ, 806, 129, doi: 10.1088/0004-637X/806/1/129

Fausnaugh, M. M., Denney, K. D., Barth, A. J., et al. 2016, ApJ, 821, 56, doi: 10.3847/0004-637X/821/1/56

Findlay, J. R., Kobulnicky, H. A., Weger, J. S., et al. 2016, PASP, 128, 115003, doi: 10.1088/1538-3873/128/969/115003

Gaskell, C. M., & Sparke, L. S. 1986, ApJ, 305, 175, doi: 10.1086/164238

Goad, M. R., Korista, K. T., De Rosa, G., et al. 2016, ApJ, 824, 11, doi: 10.3847/0004-637X/824/1/11

Gordon, K. D., Clayton, G. C., Decleir, M., et al. 2023, ApJ, 950, 86, doi: 10.3847/1538-4357/accb59

Gordon, K. D., Clayton, G. C., Misselt, K. A., Landolt, A. U., & Wolff, M. J. 2003, ApJ, 594, 279, doi: 10.1086/376774

Graham, M. J., Ross, N. P., Stern, D., et al. 2020, MNRAS, 491, 4925, doi: 10.1093/mnras/stz3244

Gunasekera, C. M., van Hoof, P. A. M., Dehghanian, M., et al. 2025, RMxAA, 61, 120, doi: 10.22201/ia.01851101p.2025.61.03.01

Homayouni, Y., Kriss, G. A., De Rosa, G., et al. 2024, ApJ, 963, 123, doi: 10.3847/1538-4357/ad1be4

IRSA. 2022, Zwicky Transient Facility Image Service, IPAC, doi: 10.26131/IRSA539

Jana, A., Ricci, C., Temple, M. J., et al. 2025, A&A, 693, A35, doi: 10.1051/0004-6361/202451058

Kaastra, J. S., Kriss, G. A., Cappi, M., et al. 2014, Science, 345, 64, doi: 10.1126/science.1253787

Kara, E., Mehdipour, M., Kriss, G. A., et al. 2021, ApJ, 922, 151, doi: 10.3847/1538-4357/ac2159

Kewley, L. J., Groves, B., Kauffmann, G., & Heckman, T. 2006, MNRAS, 372, 961, doi: 10.1111/j.1365-2966.2006.10859.x

King, A., & Pounds, K. 2015, ARA&A, 53, 115, doi: 10.1146/annurev-astro-082214-122316

Kinney, A. L., Calzetti, D., Bohlin, R. C., et al. 1996, ApJ, 467, 38, doi: 10.1086/177583

Lamer, G., Uttley, P., & McHardy, I. M. 2003, MNRAS, 342, L41, doi: 10.1046/j.1365-8711.2003.06759.x

Li, Y.-R., Wang, J.-M., & Bai, J.-M. 2016, ApJ, 831, 206, doi: 10.3847/0004-637X/831/2/206

Li, Y.-R., Wang, J.-M., Hu, C., Du, P., & Bai, J.-M. 2014, ApJL, 786, L6, doi: 10.1088/2041-8205/786/1/L6

Mao, J., Kaastra, J. S., Mehdipour, M., et al. 2022, A&A, 665, A72, doi: 10.1051/0004-6361/202142637

Markowitz, A. G., Krumpe, M., & Nikutta, R. 2014, MNRAS, 439, 1403, doi: 10.1093/mnras/stt2492

Mehdipour, M., Kriss, G. A., Kaastra, J. S., et al. 2021, A&A, 652, A150, doi: 10.1051/0004-6361/202141324

Mehdipour, M., Kaastra, J. S., Kriss, G. A., et al. 2015, A&A, 575, A22, doi: 10.1051/0004-6361/201425373

Mundell, C. G., Holloway, A. J., Pedlar, A., et al. 1995, MNRAS, 275, 67, doi: 10.1093/mnras/275.1.67

Oknyansky, V. L., Brotherton, M. S., Tsygankov, S. S., et al. 2021, MNRAS, 505, 1029, doi: 10.1093/mnras/stab1138

Peterson, B. M. 2006, in Physics of Active Galactic Nuclei at all Scales, ed. D. Alloin, Vol. 693 (Springer), 77, doi: 10.1007/3-540-34621-X_3

Peterson, B. M., Denney, K. D., De Rosa, G., et al. 2013, ApJ, 779, 109, doi: 10.1088/0004-637X/779/2/109

Proga, D., & Kallman, T. R. 2004, ApJ, 616, 688, doi: 10.1086/425117

Proga, D., Stone, J. M., & Kallman, T. R. 2000, ApJ, 543, 686, doi: 10.1086/317154

Ricci, C., & Trakhtenbrot, B. 2023, Nature Astronomy, 7, 1282, doi: 10.1038/s41550-023-02108-4

Risaliti, G., Salvati, M., Elvis, M., et al. 2009, MNRAS, 393, L1, doi: 10.1111/j.1745-3933.2008.00580.x

Runnoe, J. C., Cales, S., Ruan, J. J., et al. 2016, MNRAS, 455, 1691, doi: 10.1093/mnras/stv2385

Stern, J., & Laor, A. 2013, MNRAS, 431, 836, doi: 10.1093/mnras/stt211

Sun, M., Grier, C. J., & Peterson, B. M. 2018, PyCCF: Python Cross Correlation Function for reverberation mapping studies,, Astrophysics Source Code Library, record ascl:1805.032 http://ascl.net/1805.032

Temple, M. J., Ricci, C., Koss, M. J., et al. 2022, MNRAS, 518, 2938, doi: 10.1093/mnras/stac3279

Tody, D. 1986, in Society of Photo-Optical Instrumentation Engineers (SPIE) Conference Series, Vol. 627, Instrumentation in astronomy VI, ed. D. L. Crawford, 733, doi: 10.1117/12.968154

Tody, D. 1993, in Astronomical Society of the Pacific Conference Series, Vol. 52, Astronomical Data Analysis Software and Systems II, ed. R. J. Hanisch, R. J. V. Brissenden, & J. Barnes, 173

Torricelli-Ciamponi, G., Pietrini, P., Risaliti, G., & Salvati, M. 2014, MNRAS, 442, 2116, doi: 10.1093/mnras/stu969

Turner, T. J., Reeves, J. N., Braito, V., et al. 2018, MNRAS, 481, 2470, doi: 10.1093/mnras/sty2447

van Groningen, E., & Wanders, I. 1992, PASP, 104, 700, doi: 10.1086/133039

Wang, Y., Kaastra, J., Mehdipour, M., et al. 2022, A&A, 657, A77, doi: 10.1051/0004-6361/202141599

Zeltyn, G., Trakhtenbrot, B., Eracleous, M., et al. 2022, ApJL, 939, L16, doi: 10.3847/2041-8213/ac9a47

Zhang, X. 2026, ApJ, 1003, 130, doi: 10.3847/1538-4357/ae66f3